tween mild/moderate and severe stenoses. Second, the number of symptomatic patients was too small to support extrapolation of these preliminary findings to larger patient populations or support a multivariate analysis. However, the multiple carotid plaque characteristics that were individually observed to be significantly associated with recent symptoms in patients with mild/moderate carotid stenosis suggest that future prospective studies correlating vessel wall MR imaging with the development of thromboembolic events should include the ability to identify the presence and size of the lipid-rich necrotic core, the presence of a thin or ruptured fibrous cap, and the presence and size of intraplaque hemorrhage.

Conclusions

This in vivo 3T MR imaging of patients demonstrates several plaque components that are correlated with recent ipsilateral carotid thromboembolic symptoms. These preliminary results also suggest that the associations between plaque characteristics and symptoms may vary by degree of stenosis. If confirmed in larger studies, carotid MR imaging may distinguish stable from unstable lesions, particularly in individuals with mild/moderate carotid stenosis in whom the role of surgical intervention is currently unclear.

Acknowledgments

We thank our research technologists, Colleen A. Hammond and Scarlett R. Doyle, for their help in acquiring the MR images.

References

1. **Beneficial effect of carotid endarterectomy in symptomatic patients with high-grade carotid stenosis: North American Symptomatic Carotid Endarterectomy Trial Collaborators.** *N Engl J Med* 1991;325:445–53
2. **Randomised trial of endarterectomy for recently symptomatic carotid stenosis: final results of the MRC European Carotid Surgery Trial (ECST).** *Lancet* 1998;351:1379–87
3. Barnett HJ, Taylor DW, Eliasziw M, et al. **Benefit of carotid endarterectomy in patients with symptomatic moderate or severe stenosis: North American Symptomatic Carotid Endarterectomy Trial Collaborators.** *N Engl J Med* 1998;339:1415–25
4. Executive Committee for the Asymptomatic Carotid Atherosclerosis Study. **Endarterectomy for asymptomatic carotid artery stenosis.** *JAMA* 1995;273:1421–28
5. Halliday A, Mansfield A, Marro J, et al. **Prevention of disabling and fatal strokes by successful carotid endarterectomy in patients without recent neurological symptoms: randomised controlled trial.** *Lancet* 2004;363:1491–502
6. Golledge J, Greenhalgh RM, Davies AH. **The symptomatic carotid plaque.** *Stroke* 2000;31:774–81
7. Gao P, Chen Z, Bao Y, et al. **Correlation between carotid intraplaque hemorrhage and clinical symptoms: systematic review of observational studies.** *Stroke* 2007;38:2382–90
8. Altaf N, MacSweeney ST, Gladman J, et al. **Carotid intraplaque hemorrhage predicts recurrent symptoms in patients with high-grade carotid stenosis.** *Stroke* 2007;38:1633–35
9. Murphy RE, Moody AR, Morgan PS, et al. **Prevalence of complicated carotid atheroma as detected by magnetic resonance direct thrombus imaging in patients with suspected carotid artery stenosis and previous acute cerebral ischemia.** *Circulation* 2003;107:3053–58
10. Saam T, Cai J, Ma L, et al. **Comparison of symptomatic and asymptomatic atherosclerotic carotid plaque features with in vivo MR imaging.** *Radiology* 2006;240:464–72
11. Takaya N, Yuan C, Chu B, et al. **Association between carotid plaque characteristics and subsequent ischemic cerebrovascular events: a prospective assessment with MRI—initial results.** *Stroke* 2006;37:818–23
12. U-King-Im JM, Tang TY, Patterson A, et al. **Characterisation of carotid atheroma in symptomatic and asymptomatic patients using high resolution MRI.** *J Neurol Neurosurg Psychiatry* 2008;79:905–12. Epub 2008 Jan 10
13. Yuan C, Zhang SX, Polissar NL, et al. **Identification of fibrous cap rupture with magnetic resonance imaging is highly associated with recent transient ischemic attack or stroke.** *Circulation* 2002;105:181–85
14. Nael K, Villablanca JP, Pope WB, et al. **Supraaortic arteries: contrast-enhanced MR angiography at 3.0 T–highly accelerated parallel acquisition for improved spatial resolution over an extended field of view.** *Radiology* 2007;242:600–09
15. Hnatiuk B, Emery DJ, Wilman AH. **Effects of doubling and tripling the spatial resolution in standard 3D contrast-enhanced magnetic resonance angiography of carotid artery disease.** *J Magn Reson Imaging* 2008;27:71–77
16. DeMarco JK, Huston J, Nash AK. **Extracranial carotid MR imaging at 3T.** *Magn Reson Imaging Clin N Am* 2006;14:109–21
17. Hayes CE, Mathis CM, Yuan C. **Surface coil phased arrays for high-resolution imaging of the carotid arteries.** *J Magn Reson Imaging* 1996;6:109–12
18. Saam T, Ferguson MS, Yarnykh VL, et al. **Quantitative evaluation of carotid plaque composition by in vivo MRI.** *Arterioscler Thromb Vasc Biol* 2005;25:234–39
19. Underhill HR, Yarnykh VL, Hatsukami TS, et al. **Carotid plaque morphology and composition: initial comparison between 1.5- and 3.0-T magnetic field strengths.** *Radiology* 2008;248:550–60
20. Yarnykh VL, Yuan C. **Multislice double inversion-recovery black-blood imaging with simultaneous slice reinversion.** *J Magn Reson Imaging* 2003;17:478–83
21. Yarnykh VL, Yuan C. **T1-insensitive flow suppression using quadruple inversion-recovery.** *Magn Reson Med* 2002;48:899–905
22. Cai J, Hatsukami TS, Ferguson MS, et al. **In vivo quantitative measurement of intact fibrous cap and lipid-rich necrotic core size in atherosclerotic carotid plaque: comparison of high-resolution, contrast-enhanced magnetic resonance imaging and histology.** *Circulation* 2005;112:3437–44
23. Mitsumori LM, Hatsukami TS, Ferguson MS, et al. **In vivo accuracy of multisequence MR imaging for identifying unstable fibrous caps in advanced human carotid plaques.** *J Magn Reson Imaging* 2003;17:410–20
24. Kerwin W, Xu D, Liu F, et al. **Magnetic resonance imaging of carotid atherosclerosis: plaque analysis.** *Top Magn Reson Imaging* 2007;18:371–78
25. Chu B, Kampschulte A, Ferguson MS, et al. **Hemorrhage in the atherosclerotic carotid plaque: a high-resolution MRI study.** *Stroke* 2004;35:1079–84
26. Lovett JK, Gallagher PJ, Hands LJ, et al. **Histological correlates of carotid plaque surface morphology on lumen contrast imaging.** *Circulation* 2004;110:2190–97
27. Demarco JK, Nesbit GM, Wesbey GE, et al. **Prospective comparison of extracranial carotid stenosis with intraarterial angiography versus MR angiography using maximum-intensity projections and multiplanar reformations.** *AJR Am J Roentgenol* 1994;163:1205–12
28. Hatsukami TS, Ross R, Polissar NL, et al. **Visualization of fibrous cap thickness and rupture in human atherosclerotic carotid plaque in vivo with high-resolution magnetic resonance imaging.** *Circulation* 2000;102:959–64
29. Redgrave JN, Gallagher P, Lovett JK, et al. **Critical cap thickness and rupture in symptomatic carotid plaques: the Oxford plaque study.** *Stroke* 2008;39:1722–29. Epub 2008 Apr 10
30. Falk E. **Why do plaques rupture?** *Circulation* 1992;86(6 suppl):III30–42
31. Altaf N, Daniels L, Morgan PS, et al. **Detection of intraplaque hemorrhage by magnetic resonance imaging in symptomatic patients with mild to moderate carotid stenosis predicts recurrent neurological events.** *J Vasc Surg* 2008;47:337–42
32. Yamada N, Higashi M, Otsubo R, et al. **Association between signal hyperintensity on T1-weighted MR imaging of carotid plaques and ipsilateral ischemic events.** *AJNR Am J Neuroradiol* 2007;28:287–92
33. Eliasziw M, Streifler JY, Fox AJ, et al. **Significance of plaque ulceration in symptomatic patients with high-grade carotid stenosis: North American Symptomatic Carotid Endarterectomy Trial.** *Stroke* 1994;25:304–08
34. Morgenstern LB, Fox AJ, Sharpe BL, et al. **The risks and benefits of carotid endarterectomy in patients with near occlusion of the carotid artery: North American Symptomatic Carotid Endarterectomy Trial (NASCET) Group.** *Neurology* 1997;48:911–15

Magnetic Resonance in Medicine 64:1341–1351 (2010)

An Optimized 3D Spoiled Gradient Recalled Echo Pulse Sequence for Hemorrhage Assessment Using Inversion Recovery and Multiple Echoes (3D SHINE) for Carotid Plaque Imaging

David C. Zhu,[1–3]* Anthony T. Vu,[4] Hideki Ota,[1] and J. Kevin DeMarco[1]

Intraplaque hemorrhage into the carotid atherosclerotic plaque has been shown to create instability and progression. We have developed an optimized 3D Spoiled Gradient recalled echo pulse sequence for Hemorrhage assessment using INversion recovery and multiple Echoes (3D SHINE) for carotid plaque imaging. The sequence was developed by incorporating multiecho acquisition to its clinically validated optimized single-echo counterpart 3D inversion recovery prepared fast spoiled gradient recalled sequence. With similar scan time (4 min), 3D spoiled gradient recalled echo pulse sequence for hemorrhage assessment using inversion recovery and multiple echoes maintained comparable high-resolution volumetric coverage, black-blood effect, contrast, signal-to-noise and contrast-to-noise ratios, and similar sensitivity and specificity in detecting whether intraplaque hemorrhage was present on an artery. The multiple echoes acquired with 3D SHINE allowed the estimation of intraplaque hemorrhage T_2^* and then the subsequent characterization of intraplaque hemorrhage (T_2^* for type I < 14 msec, and for type II > 14 msec). The type I intraplaque hemorrhage size estimated by 3D SHINE was significantly and positively correlated with the size estimated manually by an expert reviewer using the histology-validated multicontrast MRI technique ($r = 0.836 \pm 0.080$, $p < 0.001$). With only one fast sequence, 3D SHINE can detect and characterize intraplaque hemorrhage that has previously required a multicontrast approach using a combination of black-blood T_1-weighted, black-blood T_2-weighted, and time-of-flight imaging techniques. Magn Reson Med 64:1341–1351, 2010. ©2010 Wiley-Liss, Inc.

Key words: carotid plaque imaging; hemorrhage; MPRAGE; IR FSPGR

In an effort to find clinically relevant markers of plaque vulnerability that increases the risk of stroke, a number of noninvasive imaging strategies have been investigated. MRI shows to be promising for imaging the carotid artery lumen and at the same time provides detailed artery wall information (1). Recent pathophysiological studies have centered on the identification and understanding of "vulnerable plaque" that poses an increased risk for thromboembolic events causing ischemia (2). Based on the previous histopathological studies of carotid endarterectomy specimens, intraplaque hemorrhage (IPH) into the carotid atherosclerotic plaque has been shown to create instability and progression as well as an association with current symptoms (3,4). An MRI technique that can successfully detect and characterize IPH is important. Such noninvasive evaluation of the in vivo appearance of carotid plaque would permit evaluation of the prospective importance of IPH to predict new ipsilateral carotid thromboembolic disease.

Previous experience at 1.5-T MR demonstrates that T_1-weighted black-blood images and 3D time-of-flight (TOF) MR angiogram (MRA) can detect IPH with good sensitivity and moderate specificity (5). The in vivo appearance of carotid IPH could be further characterized as type I or type II based on their appearance on T_2-weighted images (5,6). The classification of hemorrhage type was shown to correlate with a history of recent ipsilateral carotid thromboembolic disease (7,8). Specifically, type I hemorrhage that was characterized by decreased signal intensity compared with muscle on T_2-weighted images due to relatively short T_2 values was associated with recent symptoms. Moody et al. developed a 3D T_1-weighted magnetization prepared rapid acquisition gradient echo (MPRAGE) sequence to detect the hemorrhagic carotid plaque at 1.5 T with good sensitivity and specificity (9).

We sought to extend in vivo carotid plaque imaging from 1.5 to 3 T because recent work demonstrated the improved signal-to-noise ratio (SNR), contrast-to-noise ratio (CNR), and image quality at 3 T compared to 1.5 T for multicontrast carotid plaque imaging (10). As a part of this project to begin 3-T carotid plaque imaging, we developed a 3D inversion recovery prepared fast spoiled gradient recalled sequence (3D IR FSPGR) optimized for the detection of carotid IPH. The 3D IR FSPGR sequence was similar to the MPRAGE sequence described by Moody et al. for 1.5-T MR plaque hemorrhage imaging but optimized for 3 T. With the 3D IR FSPGR sequence we achieved a good level of success in detecting hemorrhage (11), also with improved time efficiency over the product sequence to allow high-resolution imaging of both carotid bifurcations under 5 min. Because of the short T_1 values of IPH and the T_1-weighted nature of the sequence, the 3D IR FSPGR or its equivalent counterpart 3D MPRAGE has demonstrated with improved hemorrhage CNR versus surrounding regions at 3 T comparing to 2D T_1-weighted fast

[1]Department of Radiology, Michigan State University, East Lansing, Michigan, USA.
[2]Department of Psychology, Michigan State University, East Lansing, Michigan, USA.
[3]Cognitive Imaging Research Center, Michigan State University, East Lansing, Michigan, USA.
[4]Global MR PSD/Applications Engineering, GE Healthcare, Waukesha, Wisconsin, USA.

Grant sponsors: GE Healthcare Systems and American Heart Association.

*Correspondence to: David C. Zhu, Ph.D., 358 Giltner Hall, Michigan State University, East Lansing, MI 48824, USA. E-mail: zhuda@msu.edu

Received 5 January 2010; revised 11 April 2010; accepted 28 April 2010.
DOI 10.1002/mrm.22517
Published online 22 June 2010 in Wiley Online Library (wileyonlinelibrary.com).

spin echo (FSE) and 3D TOF sequences, which are typically used in hemorrhage detection, and thus have led to improved sensitivity and specificity (12). Therefore, an optimized 3D IR FSPGR sequence can potentially be used to replace the more traditional precontrast 2D T_1-weighted FSE technique in the detection of IPH and can offer additional benefits of high-resolution volumetric visualization with 3D rendering.

With the success of the optimized 3D IR FSPGR sequence in carotid plaque detection, we further developed a sequence called 3D Spoiled Gradient recalled echo pulse sequence for Hemorrhage assessment using INversion recovery and multiple Echoes (3D SHINE) by incorporating multiple gradient echoes. This sequence includes a short echo time similar to the original 3D IR FSPGR sequence for optimal depiction of hemorrhage as well as longer echo times, which could be used to estimate the T_2^* of the hemorrhage. We hypothesized that 3D SHINE would allow us to identify IPH and further characterize the hemorrhage into types I and II based on the T_2^* value estimated from the multiple echoes.

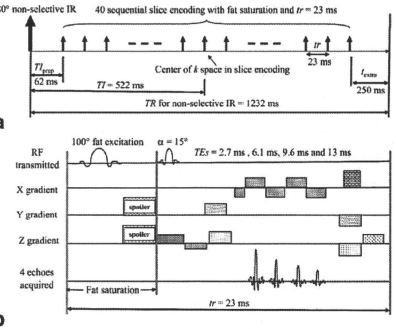

FIG. 1. The optimized 3D SHINE sequence is shown with parameters indicated, including (**a**) the overall timing diagram and (**b**) the detailed information at each slice phase encoding step.

MATERIALS AND METHODS

Pulse Sequence Development and Optimization

The 3D SHINE sequence (Fig. 1) was further developed by modifying the optimized single-echo 3D IR FSPGR that we developed on a 3T Signa® HDx MR scanner (GE Healthcare, Waukesha, WI) (11). Our goal was to provide the additional feature of T_2^* mapping of IPH without extra scan time while maintaining the same coverage, the ability in IPH detection, high-resolution volumetric acquisition, and similar level of black-blood effect. As discussed in Ref. 11, the single-echo sequence includes the following important components: a 180° nonselective Silver-Hoult adiabatic inversion recovery (IR) preparation radiofrequency (RF) pulse, an inclusion of an off-resonance fat signal saturation pulse on every encoding step and a sequential phase encoding strategy in the slice encoding direction. These components were maintained in the 3D SHINE technique. The nonselective Silver-Hoult adiabatic inversion RF pulse provides a uniform inversion of spins even in the presence of a nonuniform B_1 field and inverts spins within the entire sensitive volume of the transmit coil (13). Several fat suppression techniques were considered in this study. Spectral inversion fat nulling (a.k.a. SPECIAL, SPIR, SPAIR) technique where IR pulse is applied intermittently every few slice phase encoding steps is more time efficient than the off-resonance fat saturation technique. However, centric phase encoding is often employed to achieve optimal fat suppression, but which is in conflict with the black-blood IR pulse in combination with the sequential phase encoding strategy implemented in this work. A spatial–spectral pulse for selectively water excitation is another choice of fat signal reduction. However, spatial–spectral pulses are relatively long and thus limit the ability to shorten the echo time for the first echo. A short echo time is advantageous in IPH detection, especially in the presence of field inhomogeneity. Therefore, off-resonance fat saturation was chosen. By properly selecting the time of inversion (TI), the time of repetition (TR) with respect to the nonselective IR pulse, the data acquisition flip angle, the time of repetition in data acquisition, and the time between the RF excitation of the last slice phase encoding step and the application of the nonselective IR pulse (t_{extra}), based on the T_1 of the blood, the signal from the blood in the lumen can be minimized to reach the maximum contrast between the carotid vessel lumen and vessel wall. As TI is equal to the time from the middle of the non-selective IR pulse to acquisition of the center of k-space in the slice direction, by properly selecting the number of slice phase encoding steps, the "dead" time TI_{prep} (the time from the middle of the nonselective IR pulse to the middle of the RF pulse for the first encoding step) can be minimized.

We started the pulse sequence optimization with computer simulations using the same procedure as in our single-echo 3D IR FSPGR sequence (11) according to the basic design of the pulse sequence (Fig. 1a). In this simulation, five hypothetical tissue types with T_1 values of 500, 1000, 1500, 2000, and 2500 msec were compared. Demonstrated in Fig. 2 is the result with the parameters of TR = 23 msec, TI_{prep} = 62 msec, t_{extra} = 250 msec, flip angle = 15°, and number of slice encoding steps = 40 as indicated in Fig. 1. Stanisz et al. reported T_1 values of 1932 ± 85 msec for blood, 1412 ± 13 msec for skeletal muscle, and 1471 ± 31 msec for heart at 3 T (14). Noeske et al. reported T_1 values of 1550 ± 85 msec for blood and 1115 ± 10 msec for myocardium at 3 T (15). It is reasonable to estimate that the T_1 of blood is within the range of 1500–2000 msec, and the T_1 of vessel wall is within the range of 1000–1500 msec at 3 T. Based on these numbers, the proposed parameters should provide reasonable levels of black-blood effect. The other even

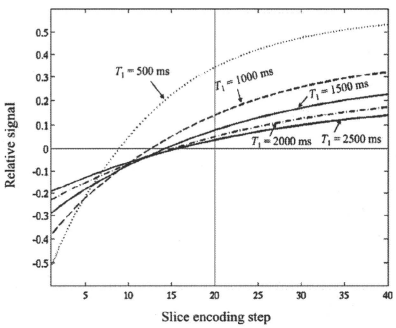

FIG. 2. Computer simulation with the scan timing parameters in Fig. 1.

more important consideration is that this technique needs to be highly sensitive to hemorrhage detection. T_1-shortening is one characteristic of hemorrhage both in the intracellular and extracellular methemoglobin state (16,17). A hypothetical T_1 of 500 msec has been used in this simulation. The simulation also shows that a range of scanning parameters can be used to provide imaging result that is sensitive to detect hemorrhage and to visualize the vessel wall. The simulations provided a guide for our protocol optimization and evaluation, but they did not provide the final parameters. Because of the relative uncertainty of the tissue T_1 values at the carotid region, the more optimized scanning parameters were achieved via studies on healthy volunteers and then confirmed on patients, as demonstrated in the Result section.

With the inclusion of multiple echo acquisitions in 3D SHINE, T_2^* values can be calculated. The T_2^* was calculated with least-square estimation based on the semi-log linear regression (18) of the voxel signal values from all echoes and their corresponding times of echo according to the following linear relationship:

$$\frac{1}{T_2^*} = -\frac{\ln S_n - \ln S_m}{\mathrm{TE}_n - \mathrm{TE}_m} \quad [1]$$

where S_n and S_m are voxel signal intensity values at echo time values of TE_n and TE_m.

The weighted-averaged images of m echoes can be obtained by

$$S_{\mathrm{ave}} = \sum_{i=1}^{m} \left(S_i \times \left(\frac{S_i}{\sum_{j=1}^{m} S_j} \right) \right) \quad [2]$$

where S_i is the signal at TE_i.

The weighted averaging is expected to increase the SNR when compared with individual echo as well as emphasizing the signal at the first echo so that the ability of hemorrhage detection is maintained.

Subjects

Three healthy subjects (Ages 31, 33, and 41, one female) participated in this study for the purpose of protocol optimization. Twenty-two patients referred by vascular surgeons or stroke neurologists with carotid stenosis between 50 and 99% measured by duplex ultrasound participated in this study. Of these patients, there were 10 patients (12 arteries) with probable carotid hemorrhagic plaque based on the single echo 3D IR FSPGR technique. We reviewed data of all the patients. However, for the detailed evaluation and demonstration of the 3D SHINE sequence, only patients with probable carotid IPH were used for data analysis (mean age ± standard deviation (SD) = 70.4 ± 8.7 years; mean weight ± SD = 87 ± 15 kg). All subjects signed consent forms approved by the Michigan State University institutional review board.

Data Acquisition

The data were collected on a 3T Signa® HDx MR scanner (GE Healthcare, Waukesha, WI) using a dedicated four-channel carotid bilateral-phased array coils (Pathway MRI, Seattle, WA). Single-echo 3D IR FSPGR image data were collected along with 3D SHINE image data for comparison. The 3D SHINE protocol was optimized by varying the t_{extra} with a minimal $\mathrm{TI}_{\mathrm{prep}}$, a sufficient coverage around bifurcation to include the range of carotid plaque typically found (11), a receiver bandwidth (rBW) without much sacrifice of SNR to allow the visualization of the bifurcation. The finalized 3D SHINE and the single-echo 3D IR FSPGR parameters used in patient data collection are listed on Table 1. More traditional quadruple inversion-recovery T_1-weighted (19), multisection double inversion-recovery T_2-weighted (20) and 3D TOF images were also collected to detect the hemorrhagic regions, and to allow independent characterization of the hemorrhage type. These procedures of hemorrhage detection and characterization have previously been validated with carotid endarterectomy specimens (5,7). The pulse sequence parameters are listed on Table 2. All data were acquired in the axial plane for image comparison. The frequency encoding was set at right–left direction to minimize the motion artifacts from swallowing, and to eliminate the potential flow artifacts introduced from the carotid artery at the other side of the neck.

Phantom Verification

The accuracy of the our finalized 3D SHINE protocol was evaluated with a phantom consisting of superparamagnetic magnetite (Fe*REX*™) (BioPhysics Assay Laboratory, Inc., Worcester, MA) water solution with the concentrations of 0.003 to 0.035 mg Fe/ml against an eight-echo 3D FSPGR sequence without RF inversion with the following parameters: TEs = 2.6, 6.1, 9.5, 13.0, 16.4, 19.9, 23.3, and 26.8 msec, time of repetition = 30.6 msec, flip angle = 15°, field of view = 16 cm, number of slices = 40, slice thickness = 1 mm, matrix size = 256 × 256, and rBW = ± 41.7 kHz. Then the data was acquired again with another eight-echo 3D FSPGR sequence by modifying the rBW to ± 62.5 kHz, echo times to 2.2, 4.6, 7, 9.4, 11.8, 14.3, 16.7, and 19.1

Table 1
Imaging Parameters for IR FSPGR and 3D SHINE

Parameter	Single-echo IR FSPGR	Four-echo 3D SHINE
Acquisition plane	Axial	Axial
1st TE (msec)	3.2	2.7
2nd TE (msec)	None	6.1
3rd TE (msec)	None	9.6
4th TE (msec)	None	13
Flip angle	15°	15°
Receiver bandwidth (kHz)	±31.25	±41.7
tr (msec)	13.7	23
TI_{prep} (msec)	45	62
Effective TI (msec)	318	522
t_{extra} (extra rest time) (msec)	0	250
TR (msec)	591	1232
Off-resonance fat saturation	Apply on every tr	Apply on every tr
Field of view	16 × 16 cm^2	16 × 16 cm^2
Matrix size	256 × 192	256 × 192
Number of slice encoding steps	40	40
Slice thickness (mm)	1	1
Slab size (mm)	36	36
Number of excitation	2	1
Scan time	3 min 50 sec	3 min 54 sec

tr, time of repetition for each phase encoding step; TI_{prep}, the time from the middle of the nonselective IR pulse to the middle of the RF pulse for the first encoding step; TR, the time of repetition with respect to the nonselective inversion; t_{extra} (extra rest time), the extra rest time after the sequence of slice phase encoding steps.

msec, and time of repetition to 22.4 msec. If the T_2^* is at the middle of the echo time range, the T_2^* estimation is expected to be most accurate. At higher T_2^* values, the first 3D FSPGR protocol is expected to provide more accurate estimation. At lower T_2^* values, the second 3D FSPGR protocol is expected to provide more accurate estimation. Data were acquired twice with each sequence. Regions of interest (ROIs) were drawn at multiple slice locations at the central slices from both acquisitions. The T_2^* values were calculated based on Eq. 1.

Patient Data Analysis

The presence and location of hemorrhage within the carotid plaque were identified by reviewing bright-blood T_1-weighted images, specifically TOF, black-blood T_1-weighted images, black-blood T_2-weighted images (5), and 3D IR FSPGR images (11,12) according to previously described techniques verified by histology. Two radiologists who were well-trained in carotid plaque detection and characterization and who were blinded to the results of the 3D SHINE reviewed all the 22 patients and reached consensus reading in all cases. Besides identifying the hemorrhage they further characterized hemorrhagic ROIs as types I and II based on T_2-weighted images based on the criteria that type I hemorrhage tends to be hypointense and type II hemorrhage tends to be isointense or hyperintense (5,7). These ROIs of types I and II were drawn at the similar anatomical locations on both the 3D IR FSPGR and 3D SHINE images. Voxel T_2^* values from these drawn ROIs were estimated from 3D SHINE images. The T_2^* values at the voxels of the types I and II ROIs from all subjects were pooled together to calculate their distributions and to test whether the T_2^* values for types I and II were statistically different from each other. To test the reliability of the 3D SHINE technique in hemorrhage characterization, a cut-off T_2^* value yielding the maximum overall accuracy was indentified from the T_2^* distributions. With this cut-off T_2^* value, the areas of type I hemorrhage were extracted from overall hemorrhagic regions on a slice-by-slice basis. Pearson's correlation analysis (standard error estimated by bootstrapping to accommodate the use of multiple slices per artery) was applied to compare type I hemorrhage areas identified based on 3D SHINE T_2^* values and those identified based on expert drawing according to T_2-weighted images. To evaluate the equivalency on hemorrhage

Table 2
Parameters for Carotid Imaging Sequences

Parameter	T_1-weighted	T_2-weighted	Time-of-flight MRA
Acquisition mode	2D	2D	3D
Acquisition sequence	Fast spin echo	Fast spin echo	Spoiled gradient and flow compensation
Blood suppression technique	Quadruple Inversion Recovery	Multisection double inversion recovery	Saturation-veins
TE (msec)	10.8	52	3.9
TR (msec)	800	4800	23
TI (msec)	520	290	N/A
Echo train length	10	12	N/A
Excitation flip angle (degrees)	90	90	20
Receiver bandwidth (±kHz)	20.83	31.25	15.63
No. of repetition	1	1	1
Field of view	160 × 160 mm^2	160 × 160 mm^2	160 × 160 mm^2
Matrix size	256 × 256	256 × 256	288 × 256
No. of slices	18	18	48
Slice thickness (mm)	2	2	1
Coverage (mm)	36	36	44
Imaging time (min:sec)	6:47	3:41	4:46

detection in sensitivity and specificity, the two radiologists also recorded and reached consensus on the presence/absence of hemorrhage based on the images of 3D IR FSPGR and then independently on the images of the first echo of 3D SHINE, without prior knowledge of whether these two sets of images belonged to a same subject or which subject they belonged to.

Image quality of the 3D SHINE data was assessed by comparing the 3D IR FSPGR images based on ROI analysis. At all the arteries with probable hemorrhages, ROIs at multiple slice locations of the 3D IR FSPGR images were drawn at the hemorrhagic region, the vessel wall outside the hemorrhagic region, the vessel lumen, the adjacent scalenus muscle, and adjacent artifact-free air region. Then the ROIs with similar sizes and locations were drawn at the first-echo of 3D SHINE. The contrast, SNR, and CNR were calculated based on an established procedure (10,21). Specifically, noise measurements were estimated from the ROI at the air region and this ROI was regarded as the noise ROI. SNR was calculated as $\text{SNR} = 0.695 \times (S_m^2 - S_n^2)^{1/2}/\sigma$, where S_m is the signal magnitude for the tissue of interest, S_n is the signal magnitude in a noise ROI, σ is the measured standard deviation of the noise, and 0.695 is the correction factor for a four-array coil design. CNR was defined as the difference between SNRs of two tissue types. The contrast of IPH versus another tissue region was calculated as $[(S_{IPH} - S_{other})/S_{other}] \times 100\%$, where S_{IPH} = signal at IPH and S_{other} = signal at other tissue. Paired t tests and correlation analyses were performed between the first-echo of 3D SHINE, the weighted average of 3D SHINE and the 3D IR FSPGR.

RESULTS

Protocol Optimization

About 36 mm (40 1-mm slices with four discarded) of coverage was needed to cover the carotid bifurcation (11). We started with ±31.25 kHz rBW (corresponding to a time of repetition of 27 msec), but a long extra recovery time (t_{extra}) would be needed to achieve a good level of black-blood effect. With the increase of rBW, we qualitatively inspected the decrease of SNRs of the first echo and weighted-average images to make sure that the image quality was qualitatively sufficient in visualizing the bifurcation. We finalized the receiver bandwidth to ±41.7 kHz (corresponding to a time of repetition of 23 msec), and then collected 3D SHINE images with various t_{extra} to quantify the black-blood effect on the three healthy volunteers. The effect of blood suppression was assessed based on the signal ratio between vessel lumen and vessel wall. With spline interpolation, an optimized t_{extra} was found at ~250 msec to maximize the lumen-wall contrast. With t_{extra} = 250 msec, the lumen/wall signal ratio at the first echo of 3D SHINE was estimated to be of 37.3%, which is lower than the 45.4 ± 9.2% from the 3D IR FSPGR protocol we have applied in our previous research (11,12).

Phantom Verification

Table 3 shows the T_2^* comparison between the eight-echo 3D FSPGR sequences (used as the standard) and the four-echo 3D SHINE sequence. T_2^* measurements from 3D SHINE varied less than 1 msec from the eight-echo 3D FSPGR sequences for T_2^* below 25 msec and less than 2 msec for T_2^* between 25 and 50 msec. However, the variation increased rapidly at high T_2^* values (>50 msec) due to the relatively lower range of echo time from 2.7 to 13 msec. However, the variation of the T_2^* measurement at high T_2^* values would not lead to misclassification of the hemorrhage type because the T_2^* threshold discriminating types I and II was found at 14 msec as discussed later.

Hemorrhage Detection and Characterization

The 3D SHINE protocol listed in the "Data Acquisition" section was the result of the optimization and was applied to patient imaging. Of the 22 patients imaged, 10 patients (12 carotid arteries) demonstrated regions of IPH based on histology-validated multicontrast MR imaging techniques, including bright-blood TOF, black-blood T_1-weighted imaging, black-blood T_2-weighted imaging, and black-blood 3D IR FSPGR. Table 4 shows the SNRs at the hemorrhagic region, the vessel wall, and the adjacent scalenus muscle region, the contrasts and CNRs of the hemorrhagic region versus lumen, wall, and muscle, as well as vessel wall versus lumen, for both 3D SHINE and its single-echo counterpart 3D IR FSPGR. For 3D SHINE, the weighted image averaging significantly improves the SNR at the hemorrhagic region, the vessel wall, and surrounding muscle. CNR of hemorrhagic region versus lumen, wall, and muscle, and the CNR of wall versus lumen were also improved with the weighted averaging strategy. Although the first echo of 3D SHINE has lower SNR and CNR when compared with 3D IR FSPGR, the weighted average of the four echoes became comparable with 3D IR FSPGR. For the first echo of 3D SHINE, the contrast of hemorrhage versus surrounding regions were comparable with 3D IR FSPGR, but it was significantly higher than the weighted average of the 3D SHINE images.

Based on the 22 patients we studied, the 3D IR FSPGR and 3D SHINE images demonstrated the same results regarding whether IPH existed on an artery. Specifically, the same 12 arteries showed probable IPH with these two imaging techniques when the reviewers evaluated both sequences in a blinded fashion. Thus, these two techniques had the same sensitivity and specificity in hemorrhage detection on an artery basis. The two sequences yielded similar IPH locations, sizes, and shapes as demonstrated by the case in Fig. 3. The two sequences show the similar nonhemorrhagic region of the plaque as well. Because of the high-resolution nature of the 3D imaging, both techniques provide the flexibility of reformatting to locate and view the IPH in various orientations.

Table 5 lists the T_2^* distribution of the types I and II regions estimated by 3D SHINE for the 10 patients participating in this study on artery basis. When reviewing all ROIs, the T_2^* values of type II hemorrhage in two (Arteries 4 and 11 in Table 5) of the 12 arteries appeared clearly as outliers. Moderate to large calcifications (10 to 40 mm^2 in area) were seen in both cases and were immediately adjacent to the type II hemorrhage ROIs.

Table 3
Phantom Comparison of T^*_2 value with Different Sequences

FeREX™ concentration (mg Fe/ml)	T^*_2 (msec) from 3D SHINE, four echoes, ±41.67 kHz rBW	T^*_2 (msec) from FSPGR, eight echoes, ±41.67 kHz rBW	T^*_2 (msec) from FSPGR, eight echoes, ±62.5 kHz rBW
0.003	69.6 ± 43.8	66.3 ± 1.8	67.3 ± 3.5
0.004	47.4 ± 9.4	48.7 ± 0.7	49.1 ± 1.6
0.005	36.6 ± 4.3	35.8 ± 0.6	35.8 ± 1.0
0.006	33.5 ± 2.8	31.7 ± 0.5	31.8 ± 0.6
0.007	28.6 ± 2.8	28.9 ± 0.4	29.1 ± 0.4
0.008	23.8 ± 2.0	23.2 ± 0.3	23.4 ± 0.6
0.009	19.7 ± 1.5	20.0 ± 0.3	20.1 ± 0.4
0.01	14.9 ± 0.9	14.4 ± 0.2	14.4 ± 0.2
0.0125	13.7 ± 0.4	13.5 ± 0.2	13.6 ± 0.1
0.015	9.0 ± 0.4	9.4 ± 0.2	9.0 ± 0.1
0.0175	8.8 ± 0.3	8.9 ± 0.2	8.7 ± 0.1
0.02	7.4 ± 0.2	8.0 ± 0.1	8.1 ± 0.2
0.03	5.3 ± 0.2	8.2 ± 0.1	5.9 ± 0.1
0.035	4.8 ± 0.1	8.4 ± 0.1	5.9 ± 0.1

rBW, receiver bandwidth.

Calcification can lead to magnetic field inhomogeneity and thus result in an underestimation of T^*_2. While there were many other examples of calcifications in the other 10 hemorrhagic carotid plaques, no additional cases of calcifications with size = 10 mm^2 were noted immediately adjacent to any other type I or II ROIs. Therefore, these two arteries with hemorrhage ROIs adjacent to moderate or large calcifications were excluded from further analysis. On a voxel-by-voxel basis, T^*_2 were 11.5 ± 3.7 msec for type I hemorrhage and 19.7 ± 9.1 msec for type II hemorrhage (statistically different at $p < 0.001$) (Fig. 4). A T^*_2 value of 14 msec (sensitivity 81.7% and specificity 70.8%) was found to discriminate most hemorrhage types. For 60 slices compared, the areas of type I hemorrhage calculated based on 3D SHINE T^*_2 values ($T^*_2 < 14$ msec) was significantly correlated with the areas of type I identified based on expert drawing according to T_2-weighted images ($r = 0.836 \pm 0.080$, $p < 0.001$) (Fig. 5).

The application of 3D SHINE is demonstrated with a carotid plaque containing both types I and II IPH, characterized by the traditional 3D TOF, the single-echo 3D IR FSPGR, T_1 and T_2-weighted FSE images. These results were found to be closely corresponding with the T^*_2 maps generated from 3D SHINE (Fig. 6). At the hemorrhage, if the T_2-weighted FSE image signal is hypointense to muscle, suggesting a type I hemorrhage, the T^*_2 value tends to be 14 msec or lower (Fig. 6b). On the other hand, if the T_2-weighted FSE image signal is iso-intense or hyperintense to muscle, suggesting a type II hemorrhage, the T^*_2 value tends to be higher than 14 msec (Fig. 6c). The 3D dataset can be reformatted to visualize the plaque from any orientation (Fig. 6a). Figure 7 shows the four echoes from 3D SHINE at TEs of 2.7, 6.1, 9.6, and 13 msec. The SNR and CNR appear to be improved through weighted averaging of the four echoes, and become comparable to those of the single-echo 3D IR FSPGR image.

DISCUSSION

The role of IPH as a potential marker for symptomatic carotid plaque had been suggested as early as 1982 by Lusby et al. (4). Their retrospective study of carotid endarterectomy specimens identified a significantly higher association of IPH in symptomatic patients when compared to asymptomatic patients. With the advancement of *in vivo* MR plaque imaging, it is now possible to prospectively evaluate IPH. One such study involved a total of 154 patients who were followed for a mean of three years after the initial in vivo carotid plaque study. In that study, IPH was shown to be statistically significantly associated with the development of new ipsilateral carotid stroke or transient ischemic attack in a prospective evaluation of asymptomatic patients with moderate carotid stenosis (22). Multiple studies using inversion-recovery T_1-weighted MPRAGE have demonstrated that recent or recurrent symptoms were associated with IPH in patients with symptomatic moderate and high-grade carotid stenosis (23–25). Patients with IPH demonstrated a more rapid increase in the size of the carotid plaques compared to those patients without hemorrhage when followed by longitudinal MRI studies (26). The potential significance of type I hemorrhage to be associated with recent symptoms was highlighted by Saam et al. (7). In that study, no significant difference was found between symptomatic and asymptomatic plaques when considering the prevalence of all types of hemorrhage. However, type I hemorrhage was found significantly more often in patients with symptomatic plaques. Conversely, the prevalence of type II hemorrhage was comparable in patients with symptomatic and those with asymptomatic plaques. This suggests the importance of identifying type I hemorrhage. This importance was also demonstrated more recently by Sadat et al. (8).

We have published a 3D IR FSPGR pulse sequence similar to the original 3D MPRAGE sequence proposed by Moody et al., but optimized for 3 T (11). When our optimized 3D IR FSPGR sequence is combined with dedicated carotid coil imaging at 3 T, it is possible to achieve high spatial resolution (~0.7 mm in-plane resolution) with sufficient coverage to visualize both carotid bifurcations in ~4 min. This high-resolution dataset supports multiplanar reformation to visualize the anatomical

Table 4
Image Quality Comparison Among 3D IR FSPGR, Preprocessed and Postprocessed 3D SHINE Images

	3D IR FSPGR	3D SHINE 1st echo	3D *SHINE* weighted average of four echoes	Paired *t* test of 3D SHINE weighted average > 1st echo	Paired *t* test of 3D SHINE weighted average < 1st echo	Correlation between 3D IR FSPGR and 1st Echo of 3D SHINE	Correlation between 3D IR FSPGR and weighted average of 3D SHINE
Hemo SNR	43.4 ± 6.5	32.0 ± 4.1	43.7 ± 5.0	$P < 0.001$			0.897 ($P < 0.001$)
Wall SNR	14.3 ± 2.1	10.9 ± 1.3	14.8 ± 1.6	$P < 0.001$			0.860 ($P < 0.001$)
Muscle SNR	11.5 ± 6.0	8.5 ± 3.8	12.7 ± 5.3	$P < 0.001$			0.816 ($P = 0.001$)
(Hemo-lumen)/lumen × 100%	626.6 ± 332.7	644.9 ± 304.2	464.4 ± 239.3		$P < 0.001$	0.969 ($P < 0.001$)	
(Hemo-wall)/wall × 100%	208.1 ± 101.6	201.4 ± 111.4	191.0 ± 103.3		$P = 0.0495$	0.929 ($P < 0.001$)	
(Hemo-muscle)/muscle × 100%	269.5 ± 91.5	264.6 ± 92.3	223.5 ± 79.6		$P < 0.001$	0.910 ($P < 0.001$)	
CNR: Hemo vs. lumen	37.5 ± 18.9	28.5 ± 13.4	37.4 ± 16.6	$P < 0.001$			0.889 ($P < 0.001$)
CNR: Hemo vs. wall	29.1 ± 4.9	21.1 ± 3.3	28.8 ± 4.2	$P < 0.001$			0.904 ($P < 0.001$)
CNR: Hemo vs. muscle	31.9 ± 5.0	23.5 ± 3.1	30.9 ± 3.8	$P < 0.001$			0.91 ($P < 0.001$)
CNR: Wall vs. lumen	8.4 ± 3.4	7.3 ± 3.4	8.6 ± 4.0	$P = 0.08$			0.641 ($P < 0.025$)

Hemo, hemorrhage region.

FIG. 3. The 3D IR FSPGR images (**a**) and the 3D SHINE weighted-average images (**b**) yield the similar locations, sizes, and shapes of the intraplaque hemorrhage (IPH) and the nonhemorrhagic region of the plaque (NHP). Because of the high-resolution nature of 3D acquisition, both techniques provide the flexibility of reformatting to locate and view the IPH in various orientations. The reformatted axial (ax), saggital (sag), and coronal (cor) views are shown.

relationship of hemorrhage with the carotid stenosis. The optimized 3D IR FSPGR highlights IPH by providing higher contrast and CNR compared with the more traditional 2D T_1-weighted FSE and 3D TOF MRA (11). The optimized 3D IR FSPGR sequence demonstrated higher

Table 5
Summary of Intraplaque Hemorrhage T^*_2 value in Patients

Patient #	Artery #	T^*_2 for type I (msec)	T^*_2 for type II (msec)
1	1	11.0 ± 3.4	19.1 ± 5.9
2	2	11.5 ± 2.4	18.5 ± 9.2
3	3		23.9 ± 7.8
4	4		6.9 ± 2.8[a]
5	5	11.2 ± 5.4	16.3 ± 11.5
5	6	8.8 ± 1.6	10.6 ± 6.1
6	7	14.4 ± 7.0	17.6 ± 6.2
7	8		23.8 ± 9.6
8	9		15.5 ± 8.1
9	10	11.1 ± 5.1	14.8 ± 4.5
9	11		8.4 ± 2.1[a]
10	12	12.8 ± 2.4	

[a]Heavy calcification was found adjacent to the hemorrhagic region.

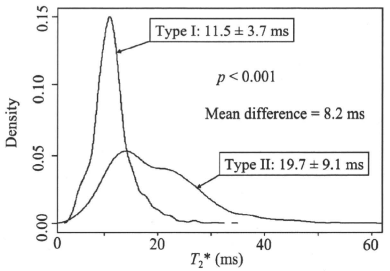

FIG. 4. Voxel-basis type I and type II T^*_2 distribution from hemorrhagic ROIs from 10 arteries in 10 patients with probable intraplaque hemorrhage.

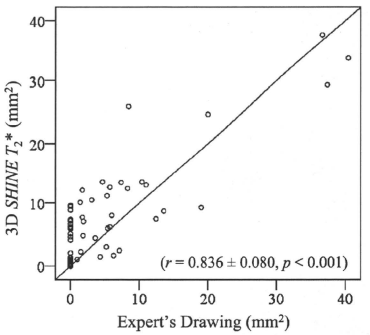

FIG. 5. On a slice-by-slice basis with a total of 60 slices, the areas of type I hemorrhage calculated based on 3D SHINE T^*_2 values (T^*_2 < 14 msec) were significantly correlated with the areas of type I estimated manually by an expert reviewer based on the signal intensity of the T_2-weighted images.

diagnostic capability for the detection and quantification of IPH compared with 2D T_1-weighted FSE and 3D TOF MRA based on histological evaluation of the carotid endarterectomy specimen (12). The 3D SHINE sequence presented in this work has been able to maintain the contrast, CNR of the 3D IR FSPGR single-echo counterpart within approximately the same scan time. Judging on whether IPH is present or absent on an artery, the sensitivity and specificity for the detection of IPH were the same comparing 3D SHINE with the previously

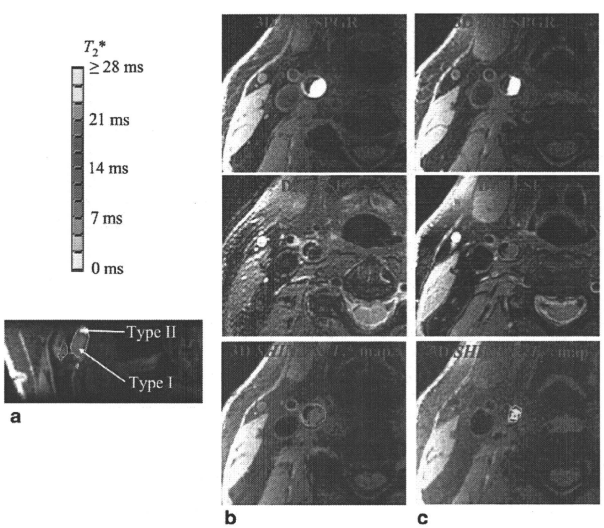

FIG. 6. An intraplaque hemorrhage with both type I and type II hemorrhagic regions is shown. The high-contrast hemorrhagic region is clearly depicted by 3D IR FSPGR or 3D SHINE. The T^*_2 value is color coded with the bar at the upper-left corner. The type I hemorrhage tends to have a T^*_2 value below 14 msec, and type II hemorrhage tends to have a T^*_2 value above 14 msec. The two hemorrhage types are shown clearly in the reformatted coronal view (**a**). Consistent with the results from 3D SHINE, (**b**) type I hemorrhage (shown are axial slices at predominately type I region) appears to be hypointense in DIR FSE, and (**c**) type II hemorrhage (shown are axial slices at predominately type II region) appears to be iso-intense in DIR FSE.

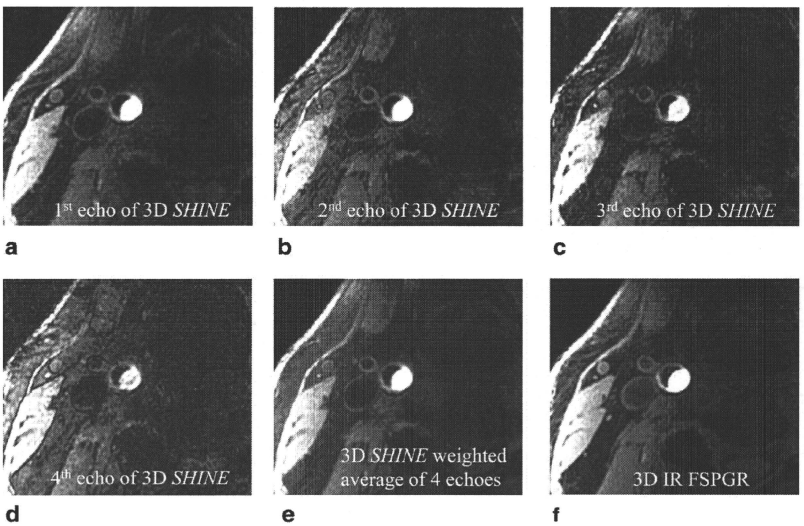

FIG. 7. The four images at the echoes with TEs of (**a**) 2.7 msec, (**b**) 6.1 msec, (**c**) 9.6 msec, and (**d**) 13 msec from 3D SHINE are shown. **e**: The SNR is improved with the weighted average of the four echoes and appears comparable to the SNR of the single-echo 3D IR FSPGR image (**f**).

histology-validated 3D IR FSPGR sequence. Their equivalence is also demonstrated by the case study shown in Fig. 3. The 3D SHINE technique will be able to replace the 3D IR FSPGR single-echo technique. In addition, the 3D SHINE sequence provides the valuable addition of T_2^* mapping, which in-turn can characterize the hemorrhage type with approximately the same imaging time compared with its 3D IR FSPGR single-echo counterpart. Our data suggest that a T_2^* threshold of 14 msec provides the best overall accuracy in hemorrhage characterization. Based on this threshold, the type I size characterized by 3D SHINE T_2^* maps was significantly and positively correlated with the size estimated manually by an expert reviewer. We must add the caveat that the size of the dataset was limited. The type I hemorrhage size estimation and T_2^* threshold identification were based on a same dataset. However, small variation of the T_2^* threshold, which leads to the change of the hemorrhage size estimation in the same direction, should not change the trend of the type I hemorrhage size estimated by 3D SHINE and its positive correlation with the size estimated manually by an expert reviewer. This correlation validated the reliability of the 3D SHINE technique in hemorrhage characterization. Although a binary method based on a single threshold is easy to be adopted in clinical practice, it is not ideal because IPH types differ in a continuous manner. With enough data, the correlation between symptom and T_2^* distribution within IPH can be established, and thus a statistical prognosis can potentially be established.

Our four-echo 3D SHINE protocol was optimized to identify type I hemorrhage, the type of hemorrhage that has been shown to be associated with thromboembolic events (7), by applying the range of echo time values from 2.7 to 13 msec. The estimation of the T_2^* values outside this echo time range tends to be less accurate. Based on our phantom study, the inaccuracy was limited to less than 1 msec for T_2^* below 25 msec when comparing the results from our 3D SHINE sequence with the eight-echo FSPGR sequence. Also, the standard deviation of the T_2^* measurement estimated by the 3D SHINE were about 6% between T_2^* of 13 and 24 msec, and less than 5% for $T_2^* < 13$ msec. The disagreement in T_2^* estimated by 3D SHINE compared with the eight-echo FSPGR sequence and the SD of the T_2^* measurement by 3D SHINE increased rapidly at T_2^* value over 50 msec. These inaccuracy and variation would not lead to the misclassification of the hemorrhage types as the cutoff between types I and II was found to be ~14 msec, unless the T_2^* happened to be in the range of 13 to 14 msec. Phantom study on Table 3 shows that a higher number of echoes can reduce the variation of estimation for T_2^* of less than 40 msec, the range of the IPH T_2^* distribution found in our work (Fig. 4). Assuming the receiver bandwidth and the data acquisition scheme are maintained, the increase in the number of echo would lead to the increase of

required extra recovery time (t_{extra}) to achieve a similar level of black-blood effect, and thus the increase of scan time. As T_2^* estimation was quite accurate and precise for T_2^* below 25 msec (Table 3) and the threshold T_2^* for discriminating the IPH types was around 14 msec, adding more echoes might not improve IPH characterization, but at the expense of longer scan time. Validation of the 3D SHINE sequence in detecting and quantifying the volumes of types I and II hemorrhage with histological analysis of carotid endarterectomy specimens is still ongoing.

One limitation of the 3D SHINE technique is that it is prone to the effect of magnetic field inhomogeneity in hemorrhage characterization. This happens when there is calcification within or right next to the hemorrhagic region. Basically, the T_2^* is shortened due to magnetic field inhomogeneity at or near the calcification, and thus type II hemorrhage can be mis-classified as type I. In this study, moderate or large calcifications (10–40 mm^2) were noted immediately adjacent to the hemorrhage in two arteries. With the 14 msec T_2^* threshold we found, the probable type II hemorrhage in these two arteries would have been mis-classified as type I hemorrhage. While the calcifications were the main sources affecting T_2^* estimation at IPH based on our data, any field inhomogeneity, such as poor shimming, can affect T_2^* estimation and thus lead the mis-classification of type II hemorrhage to type I hemorrhage. High-order shimming (27), although having not been used in the data acquired in this work, will be useful in reducing the static field inhomogeneity. As type I but not type II hemorrhage is significantly associated with recent symptoms (7), the misclassification of type II to type I will inherently make the 3D SHINE technique more conservative. However, its ability of hemorrhage detection is comparable to 3D IR FSPGR due to the short echo time of its first echo. Histological correlation has demonstrated that heavy calcification in some rare cases can lead to the failure of hemorrhage detection for 3D IR FSPGR (12). This failure would likely occur with 3D SHINE as well. An even shorter first echo time, through an excitation RF pulse with a shorter duration (A 0.36-msec short RF pulse was already applied in 3D SHINE.) and/or the shift of the center of k_x space, can be beneficial in this aspect. The effect of calcification on the characterization of IPH into type I and type II using 3D SHINE has not been fully quantified and further research with histological correlation is on-going. T_2-weighted FSE images, which are less affected by the magnetic field inhomogeneity, should also be acquired as a complementary to 3D SHINE. When there is inconsistency found between 3D SHINE images and T_2-weighted FSE images, the IPH characterization based on T_2-weighted FSE images should be used.

The 3D SHINE technique was developed for IPH detection and characterization at the carotid artery. It can be used to visualize the stenosis. However, it is still necessary to use other standard sequences (black-blood T_1-weighted precontrast and postcontrast, black-blood T_2-weighted, and bright-blood 3D TOF) to extract other plaque components, such as fibrous cap and lipid-rich necrotic core. It may be possible to reduce the overall scan time by deleting the precontrast black-blood T_1-weighted sequence and using the information from the first echo of the 3D SHINE sequence instead. The 3D SHINE technique is directly applicable to other anatomical sites where motion artifacts are not issues, such as the femoral arteries. For sites suffering image motion artifacts, such as the coronary arteries, the 3D SHINE sequence needs to be implemented with a motion-correction technique such as the application of a navigator echo.

As discussed earlier, the 3D SHINE sequence was optimized with the 3D IR FSPGR single-echo sequence as a reference. We did not attempt a global optimization of parameters. The choice of number of echo has been discussed earlier. A few other parameters are further discussed following with respect to optimization. A 180° flip angle was chosen for the non-selective IR in the 3D SHINE protocol. If a non-180° flip angle is used, the null point for the blood signal would occur at an earlier slice phase encoding step (Fig. 2). As a slice sequential phase encoding scheme is applied, a longer extra recovery time (t_{extra}) would be needed. Thus a 180° flip angle is the best choice in terms of scan time efficiency. The TI_{prep} has already been set at the minimum limited by the RF and gradient pulse widths. The scan time efficiency (setting t_{extra} to zero) has been considered by dividing the slice phase encoding steps to two or more nonselective IR applications while still with the blood signal nulled. However, simulation shows a proportional drop of the relative signal (drop to ~50% of the relative signal generated with the protocol shown in Fig. 2 if two IR applications are used), and thus the drop of image SNR. A longer t_{extra} provides extra time for signal recovery and thus higher SNR. Similarly, the rBW was chosen based on conflicting benefits of image SNR and scan time efficiency. The decrease of rBW increases the SNR, but a longer t_{extra} (and thus a longer scan time) would be needed to set the blood signal null point at the center of the k space. The increase of rBW leads to a shorter t_{extra} (and thus a shorter scan time) to achieve similar black-blood effect, but the image SNR would drop. As our single-echo 3D IR FSPGR sequence has been validated in previous studies (11,12), its rBW became the reference for the manipulation of the rBW for 3D SHINE. As demonstrated in the results, the 3D SHINE weighted-average images achieved similar SNRs with its single-echo 3D IR FSPGR counterpart. Therefore, we relied on the manipulation of the t_{extra} to qualitatively maximize the contrast between the lumen and wall. Lastly, 3D SHINE images were acquired in axial plane for easy image comparison in this work. The black-blood effect allows data acquisition at a coronal plane without flow artifacts from the artery at the other side of the neck, and potentially with a larger coverage of the carotid arteries.

In summary, the optimized 3D SHINE technique can detect and characterize carotid IPH. The 3D SHINE images can also provide high-quality visualization at any direction through multiplanar reformation to localize the abnormal regions. This sequence satisfies multiple functions in carotid plaque imaging with one 4-min scan. The 3D SHINE technique also eliminates the issue of image misregistration when comparing images from multiple sequences. The relatively short examination time,

high sensitivity in hemorrhage detection, the ability to characterize type I and type II hemorrhage, as well as the possibility of inherent high-quality multiplanar reformations due to the 3D volumetric acquisition with submillimeter resolution should greatly facilitate the acceptance of the 3D SHINE technique in a busy clinical practice. With the advantages of the 3D SHINE technique, a semiautomated quantification of IPH is currently under development to systematically quantify and characterize the progression of the hemorrhage. This further development can potentially be used as an objective tool in multi-site clinical trials as well as longitudinal carotid plaque studies.

ACKNOWLEDGMENTS

The authors thank Dr. Vasily Yarnykh for providing the original QIR T_1-weighted and DIR T_2-weighted sequence source codes and Ms. Colleen Hammond and Ms. Scarlett Doyle for scanning support.

REFERENCES

1. Yuan C, Kerwin WS. MRI of atherosclerosis. J Magn Reson Imaging 2004;19:710–719.
2. Shah PK. Mechanisms of plaque vulnerability and rupture. J Am Coll Cardiol 2003;41(4 Suppl S):15S–22S.
3. Fryer JA, Myers PC, Appleberg M. Carotid intraplaque hemorrhage: the significance of neovascularity. J Vasc Surg 1987;6:341–349.
4. Lusby RJ, Ferrell LD, Ehrenfeld WK, Stoney RJ, Wylie EJ. Carotid plaque hemorrhage. Its role in production of cerebral ischemia. Arch Surg 1982;117:1479–1488.
5. Chu B, Kampschulte A, Ferguson MS, Kerwin WS, Yarnykh VL, O'Brien KD, Polissar NL, Hatsukami TS, Yuan C. Hemorrhage in the atherosclerotic carotid plaque: a high-resolution MRI study. Stroke 2004;35:1079–1084.
6. Kampschulte A, Ferguson MS, Kerwin WS, Polissar NL, Chu B, Saam T, Hatsukami TS, Yuan C. Differentiation of intraplaque versus juxtaluminal hemorrhage/thrombus in advanced human carotid atherosclerotic lesions by in vivo magnetic resonance imaging. Circulation 2004;110:3239–3244.
7. Saam T, Cai J, Ma L, Cai YQ, Ferguson MS, Polissar NL, Hatsukami TS, Yuan C. Comparison of symptomatic and asymptomatic atherosclerotic carotid plaque features with in vivo MR imaging. Radiology 2006;240:464–472.
8. Sadat U, Weerakkody RA, Bowden DJ, Young VE, Graves MJ, Li ZY, Tang TY, Gaunt ME, Hayes PD, Gillard JH. Utility of high resolution MR imaging to assess carotid plaque morphology: a comparison of acute symptomatic, recently symptomatic and asymptomatic patients with carotid artery disease. Atherosclerosis 2009;207:434–439.
9. Moody AR, Murphy RE, Morgan PS, Martel AL, Delay GS, Allder S, MacSweeney ST, Tennant WG, Gladman J, Lowe J, Hunt BJ. Characterization of complicated carotid plaque with magnetic resonance direct thrombus imaging in patients with cerebral ischemia. Circulation 2003;107:3047–3052.
10. Yarnykh VL, Terashima M, Hayes CE, Shimakawa A, Takaya N, Nguyen PK, Brittain JH, McConnell MV, Yuan C. Multicontrast black-blood MRI of carotid arteries: comparison between 1.5 and 3 tesla magnetic field strengths. J Magn Reson Imaging 2006;23:691–698.
11. Zhu DC, Ferguson MS, DeMarco JK. An optimized 3D inversion recovery prepared fast spoiled gradient recalled sequence for carotid plaque hemorrhage imaging at 3.0 T. Magn Reson Imaging 2008;26:1360–1366.
12. Ota H, Yarnykh VL, Ferguson MS, Underhill HR, Demarco JK, Zhu DC, Oikawa M, Dong L, Zhao X, Collar A, Hatsukami TS, Yuan C. Carotid intraplaque hemorrhage imaging at 3.0-T MR imaging: comparison of the diagnostic performance of three T1-weighted sequences. Radiology 2010;254:551–563.
13. Silver M, Joseph R, Hoult D. Highly selective $\pi/2$ and π pulse generation. J Magn Reson 1984;59:347–351.
14. Stanisz GJ, Odrobina EE, Pun J, Escaravage M, Graham SJ, Bronskill MJ, Henkelman RM. T1, T2 relaxation and magnetization transfer in tissue at 3T. Magn Reson Med 2005;54:507–512.
15. Noeske R, Seifert F, Rhein KH, Rinneberg H. Human cardiac imaging at 3 T using phased array coils. Magn Reson Med 2000;44:978–982.
16. Allkemper T, Tombach B, Schwindt W, Kugel H, Schilling M, Debus O, Mollmann F, Heindel W. Acute and subacute intracerebral hemorrhages: comparison of MR imaging at 1.5 and 3.0 T--initial experience. Radiology 2004;232:874–881.
17. Gomori JM, Grossman RI. Mechanisms responsible for the MR appearance and evolution of intracranial hemorrhage. Radiographics 1988;8:427–440.
18. Miller I, Freund JE, Johnson RA. Probability and statistics for engineers, 4th ed. New Jersey: Prentice Hall; 1990.
19. Yarnykh VL, Yuan C. T1-insensitive flow suppression using quadruple inversion-recovery. Magn Reson Med 2002;48:899–905.
20. Yarnykh VL, Yuan C. Multislice double inversion-recovery black-blood imaging with simultaneous slice reinversion. J Magn Reson Imaging 2003;17:478–483.
21. Constantinides CD, Atalar E, McVeigh ER. Signal-to-noise measurements in magnitude images from NMR phased arrays. Magn Reson Med 1997;38:852–857.
22. Takaya N, Yuan C, Chu B, Saam T, Underhill H, Cai J, Tran N, Polissar NL, Isaac C, Ferguson MS, Garden GA, Cramer SC, Maravilla KR, Hashimoto B, Hatsukami TS. Association between carotid plaque characteristics and subsequent ischemic cerebrovascular events: a prospective assessment with MRI–initial results. Stroke 2006;37:818–823.
23. Altaf N, Daniels L, Morgan PS, Auer D, MacSweeney ST, Moody AR, Gladman JR. Detection of intraplaque hemorrhage by magnetic resonance imaging in symptomatic patients with mild to moderate carotid stenosis predicts recurrent neurological events. J Vasc Surg 2008;47:337–342.
24. Altaf N, MacSweeney ST, Gladman J, Auer DP. Carotid intraplaque hemorrhage predicts recurrent symptoms in patients with high-grade carotid stenosis. Stroke 2007;38:1633–1635.
25. Yamada N, Higashi M, Otsubo R, Sakuma T, Oyama N, Tanaka R, Iihara K, Naritomi H, Minematsu K, Naito H. Association between signal hyperintensity on T1-weighted MR imaging of carotid plaques and ipsilateral ischemic events. Am J Neuroradiol 2007;28:287–292.
26. Takaya N, Yuan C, Chu B, Saam T, Polissar NL, Jarvik GP, Isaac C, McDonough J, Natiello C, Small R, Ferguson MS, Hatsukami TS. Presence of intraplaque hemorrhage stimulates progression of carotid atherosclerotic plaques: a high-resolution magnetic resonance imaging study. Circulation 2005;111:2768–2775.
27. Kim DH, Adalsteinsson E, Glover GH, Spielman DM. Regularized higher-order in vivo shimming. Magn Reson Med 2002;48:715–722.

Magnetic Resonance in Medicine 64:567–573 (2010)

Localized Measurement of Atherosclerotic Plaque Inflammatory Burden With Dynamic Contrast–Enhanced MRI

Huijun Chen,[1] Jianming Cai,[2] Xihai Zhao,[1] Hunter Underhill,[1] Hideki Ota,[1] Minako Oikawa,[1] Li Dong,[1] Chun Yuan,[1] and William S. Kerwin[1]*

Inflammation plays an important role in progression and rupture of atherosclerotic plaque. Dynamic contrast–enhanced MRI has been proposed as a tool to evaluate inflammation in vivo by measuring the transfer constant and partial plasma volume, which are influenced by inflammation. This study sought to demonstrate the ability of dynamic contrast–enhanced MRI to provide localized measurements of transfer constant and partial plasma volume within plaque regions of different compositions. In order to do that, a highly automatic procedure for localized measurement of dynamic contrast–enhanced MRI parameters was developed. In 47 subjects, the average transfer constant and partial plasma volume were highest in loose matrix and fibrous tissue and substantially lower in intraplaque hemorrhage, lipid rich/necrotic core, and calcification. In addition, except for hemorrhage and calcification, statistically significant differences of transfer constant and partial plasma volume were observed for any pair of these components. This suggests that transfer constant and partial plasma volume could be helpful to differentiate different plaque components and that dynamic contrast–enhanced MRI has the potential to assess inflammatory burden in specific regions. Magn Reson Med 64:567–573, 2010. © 2010 Wiley-Liss, Inc.

Key words: dynamic contrast–enhanced MRI; atherosclerosis; carotid artery; kinetic model; inflammation

Inflammation is important in both the pathogenesis and outcome of atherosclerosis and is associated with fibrous cap rupture (1,2). Plaque inflammation may have multiple effects that weaken plaque structural integrity, including inhibition of new collagen production and dissolution of existing fibrous matrix by matrix metalloproteinases (3). Thus, noninvasive methods to quantify plaque inflammation in atherosclerosis plaque could be valuable for identifying plaques at increased risk for rupture.

Recently, ^{18}F-fluorodeoxyglucose, which is a glucose analog that is taken up by cells in proportion to their metabolic activity (4), has been used to detect atherosclerotic plaque inflammation with positron emission tomography. Elevated ^{18}F-fluorodeoxyglucose positron emission tomography signal shows increased glucose metabolism associated with macrophages, a key inflammatory marker.

High resolution MRI with injection of gadolinium contrast agents offers another approach for evaluating inflammation in vivo. The degree of enhancement of fibrous regions has been found to relate to the amount of neovasculature (5), which is a key pathway for inflammatory cell infiltration. Furthermore, dynamic contrast–enhanced MRI (DCE-MRI) has been shown to be sensitive to inflammatory content within plaque (6). Model-based estimates of transfer constant (K^{trans}) and the fractional plasma volume (v_p) produced from kinetic analysis of DCE-MRI quantify the increased vascular supply and permeability that support macrophage metabolism. Thus, DCE-MRI has a similar interpretation to ^{18}F-fluorodeoxyglucose positron emission tomography regarding macrophage metabolism. In fact, Calcagno et al. (7) showed that the DCE-MRI and ^{18}F-fluorodeoxyglucose positron emission tomography parameters both have positive correlation with neovessel count in a rabbit model of atherosclerotic plaque.

A potential advantage of DCE-MRI is that it provides relatively high (<1 mm) spatial resolution, which may allow DCE-MRI to generate measurements of inflammatory burden localized to key regions within the plaque. In previous studies, however, only the mean measurements of the whole plaque were investigated. Mean values are less sensitive to noise and partial-volume artifacts caused by technical limitations of DCE-MRI, but mean values fail to provide critical location information. For instance, inflammation in the plaque shoulders may be more destabilizing than inflammation deep within the plaque. The question of whether the current spatial resolution and image quality of DCE-MRI are high enough to evaluate localized characteristics is unknown.

In this study, we sought to demonstrate the ability of DCE-MRI to provide localized measurements by comparing K^{trans} and v_p of contrast agent uptake across plaque regions with different compositions. We hypothesized that different plaque components would be associated with different values of K^{trans} and v_p, reflecting the varying vascularities and permeabilities of each region. A highly automatic procedure to generate the colorized vasa vasorum image (V-V image), presenting K^{trans} and v_p with green and red, was established. To map components contours from standard weightings to DCE-MRI

[1]Department of Radiology, University of Washington, Seattle, Washington, USA.

[2]Department of Radiology, PLA General Hospital, Beijing, China.

*Correspondence to: William S. Kerwin, Ph.D., 815 Mercer Street, Box 358050, Seattle, WA 98109. E-mail: bkerwin@u.washington.edu

Received 5 June 2009; revised 24 November 2009; accepted 8 January 2010.

DOI 10.1002/mrm.22369

Published online in Wiley InterScience (www.interscience.wiley.com).

Table 1
Summary of the Relevant Imaging Parameters in MRI Acquisition Protocol

	DCE	T_1-weighted, contrast-enhanced T_1-weighted	Time of flight	Proton density–weighted	T_2-weighted
TR (ms)	100	800	29	Variable*	Variable*
TE (ms)	6.2	8.8	2.1	13.1	56.9
Slice thickness (mm)	2	2	2	2	2
Gap between slices (mm)	0	0	0	0	0
Matrix	256 × 192	256 × 256	256 × 256	256 × 256	256 × 256
Field of view (mm)	140 × 112	140 × 112	140 × 112	140 × 112	140 × 112

*Proton density–weighted and T_2-weighted: pulse repetition time = three or four cardiac R-R intervals.

images, two steps of registration algorithms were also developed to deal with the mismatch between them automatically.

MATERIALS AND METHODS

Study Population

A total of 55 subjects (age: 66.36 ± 11.99) were randomly selected after informed consent was obtained. The inclusion criterion was more than 50% stenosis by duplex ultrasound examination. The study procedures and consent forms were reviewed and approved by the institutional review board. There were 48 male subjects and seven female subjects.

MRI Protocol

Images were acquired from all subjects on a 3-T MR scanner (Signa; General Electric Healthcare, Milwaukee, WI). A custom-built, phased-array carotid coil was used to improve signal-to-noise performance. The examination included a DCE-MRI sequence consisting of axial two-dimensional spoiled gradient recalled echo imaging without cardiac gating. Data were simultaneously acquired at six contiguous 2mm-thick locations, centered on the bifurcation of the index carotid artery, and at 12 time points separated by a repetition interval of 19 sec. Index side was assigned as the symptomatic side for the symptomatic patients and the artery with greater stenosis for each asymptomatic patient. Symptomatic status was obtained from the clinical history of the patient and was defined as amaurosis fugax, transient ischemic attacks, or overt stroke. Coincident with the second image in the sequence, 0.1 mmol/kg of a gadolinium-based contrast agent (Omniscan; General Electric Healthcare Canada, Mississauga, Ontario, Canada) was injected at a rate of 2 mL/sec by a power injector. The use of a spoiled gradient recalled echo sequence produced a T_1-dependent signal within the imaging slice. To impose a T_1-dependent signal on inflowing blood, spatial saturation bands with width of 80mm were used and resulted in dark blood on images prior to contrast bolus arrival. The saturation bands were arranged at the proximal and distal ends of the acquisition slab, with gaps of 5 mm.

Before and after the injection of contrast agent, an axial T_1-weighted fast spin echo sequence with a quadruple inversion recovery black-blood preparation (8) was applied to obtain precontrast T_1-weighted and contrast-enhanced T_1-weighted images. Other contrast weightings acquired with a standard protocol (9) included time-of-flight, T_2-weighted, and proton density–weighted images. The imaging sequences were as follows: time of flight: fast gradient echo; T_2-weighted and proton density–weighted: double echo, cardiac-gated. Relevant imaging parameters are summarized in Table 1.

Image Analysis

Lumen/Wall and Components Identification

Based on a standard review protocol of multicontrast MRI validated with histology (10), one expert reader (X.Z.) blinded to DCE results reviewed all the images of standard weightings. Then all the cases were randomly distributed among the other three readers (H.U., H.O., M.O.) to be peer reviewed. If the peer reviewer had different opinions, the final decision was made by consensus of the two reviewers. Analyses were performed using the semiautomatic analysis software CASCADE (11), wherein the readers identified the lumen and outer wall boundaries of the carotid artery and lipid rich/necrotic core (NC), calcification (CA), hemorrhage (Hem), and loose matrix (LM) regions within the plaque. Unclassified regions within the plaque wall were considered to be fibrous tissue (FIB). The lumen and wall boundaries were represented by B-splines and the components were manually drawn.

Initial Registration of DCE-MRI and Other Weightings

After the compositional analysis, parametric images of K^{trans} and v_p were automatically generated from the DCE-MRI results. To automatically extract the arterial input function (AIF) and define the analysis region of interest for generation of these images, an initial three-dimensional registration of the DCE-MRI series and standard contrast weightings is required, in order. An automated registration algorithm was devised that searches for the optimal z-direction shift (*sz*), in-plane shift (*sx*, *sy*) and contour scaling to maximize the function

$$\sum_{i=1}^{3} Energy(C_i) \quad [1]$$

where C_i is the sets of points making up the lumen contour in slice i ($i = 1$, the contours of slice before bifurcation; $i = 2$, the bifurcation slice; and $i = 3$, the slice after bifurcation). The energy function is given by

$$Energy(C) = \oint_{(x,y)\in C_a} \left| \vec{G}_{z+sz}(x - sx, y - sy) \times \vec{C}_a(x,y) \right| * E_{z+sz}(x,y) \quad [2]$$

where $\vec{G}_z$ (x, y) is the intensity gradient vector of the DCE-MRI image at *zth* slice. Contour C_a is the scaled C with scaling factor a ($a = -0.5$, shrink 0.5 mm; $a = 0$, original contour; $a = 0.5$, expand 0.5 mm). $\vec{C}_a$ (x, y) is the unit vector function representing the direction of tangent at point (x, y) of contour C_a. E_z (x, y) is the edge energy function of the DCE-MRI image at *zth* slice. To generate the edge energy function, edges were produced by Canny Edge detector and then blurred by two-dimensional gaussian filter. The calculated location shift was automatically applied, and the in-plane shift is stored and will be used as the initial shift for mapping boundaries.

Generation of Parametric Image From DCE-MRI

After initial registration, the method described by Kerwin et al. (12) was used to automatically generate parametric images of K^{trans} and v_p. This approach uses a two-compartment kinetic model to characterize contrast agent concentration according to the differential equation

$$\dot{C}_t(t) = v_p \dot{C}_p(t) + K^{trans} C_p(t) \quad [3]$$

where $C_t(t)$ and $C_p(t)$ are the contrast agent concentration functions in the tissue and blood plasma, respectively. These two functions are approximated by the change in signal intensity of DCE-MRI due to contrast agent in the tissue and artery over time and used to solve for K^{trans} and v_p.

A critical component of the model is the AIF $C_p(t)$, which must either be determined from the DCE-MRI results directly or from a population model. In this study, both approaches were used and compared to understand the influence of the AIF on the results. First, a single AIF was automatically extracted for each subject from all slices in a small region around the center of the blood vessel, using a clustering algorithm (12). This approach minimizes the influence of partial-volume artifacts and flow artifacts by selecting only those pixels with high and rapid enhancement and then averages their intensity curves to obtain the AIF.

One drawback of this approach is that signal enhancement generally underestimates concentration in the blood due to factors such as T_2^* shortening affecting the spoiled gradient recalled echo acquisition, thereby leading to an inaccurate AIF (13). This effect is particularly problematic at bolus arrival when the peak concentration occurs. To address this concern, we also performed the kinetic analysis a second time with a model-based universal AIF for the whole population. This population-derived AIF is assumed to have a biexponential decay:

$$C_p(t) = \begin{cases} 0, & t < t_0 \\ D(a_1 \exp(-m_1(t - t_0)) + a_2 \exp(-m_2(t - t_0))), & t \geq t_0 \end{cases} \quad [4]$$

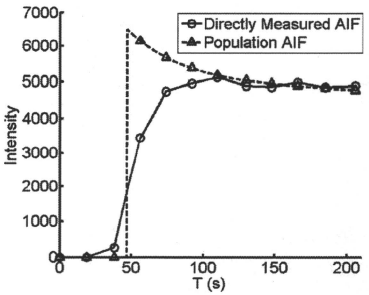

FIG. 1. The directly measured AIF and the corresponding population-derived AIF used for the case shown in Fig. 2.

where $a_1 = 3.51866$ *kg/L*, $a_2 = 13.0023$ *kg/L*, $m_1 = 1.7746$ min^{-1}, and $m_2 = 0.0267735$ min^{-1} (14). The bolus arrival time t_0 is aligned to the arrival time of the directly measured AIF. Finally, the population-derived AIF is scaled by setting the value of D such that the difference between the last five points of the population curve and the measured AIF is minimized, under the assumption that at later times, the nonlinearities of the enhancement versus concentration relationship are less problematic. Figure 1 shows an example of the directly measured AIF and the corresponding scaled population-derived AIF.

After $C_p(t)$ is extracted, K^{trans} and v_p are computed for every pixel in a 4-cm × 4-cm region of interest centered on the carotid artery, and the results are displayed in a colorized image, with v_p in the red channel and K^{trans} in the green channel. Thus, regions with blood, such as the carotid artery lumen, appear red and regions with rapid transfer appear green (Fig. 2f,g). We refer to this colorized image as a V-V image.

Mapping Boundaries and Computing Average K^{trans} and v_p of Components

After computing the V-V images, the slice correspondence between the V-V images and the other contrast weightings was visually verified and adjusted up or down as necessary. Then, the boundaries of the lumen, outer wall, and components drawn on the corresponding other weightings were automatically mapped to the V-V image by refining the in-plane registration. The lumen boundary was first mapped to the V-V image, with the in-plane shift determined during the initial location registration. To account for small remaining misregistration, the algorithm searched over a small region to maximize the function

$$\int\int_{(x,y)\in L} v_p(x + dx, y + dy) \quad [5]$$

where L is the region inside the lumen boundary, and dx and dy are the in-plane shifts to be found. The outer wall and components boundary were then mapped to

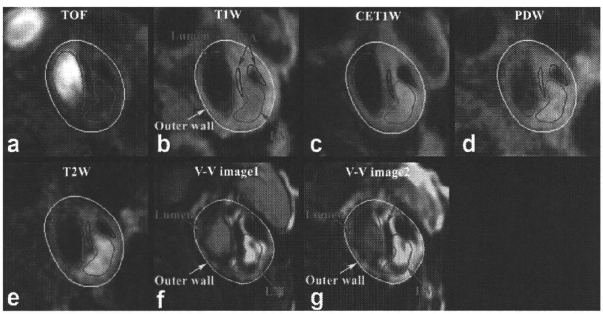

FIG. 2. One example of mapping contours of lumen, outer wall, and plaque components (arrows) from other weightings onto produced V-V image. **a:** Time of flight, **(b)** T_1-weighted, **(c)** contrast-enhanced T_1-weighted, **(d)** proton density–weighted, **(e)** T_2-weighted, **(f)** produced V-V image using directly measured AIF, **(g)** produced V-V image using population-derived AIF.

and displayed on the V-V image, using the same shift obtained by the lumen registration. Further manual shifting was then allowed in case of registration failure. Small manual adjustments in the lumen and outer wall contours were also allowed by manipulating the node points of the B-spline when the vessel shape in the V-V image was not well matched to the standard weightings. The component contours were not adjusted. An example of the contour mapping is shown in Fig. 2.

Once all the contours have been mapped, the average values of K^{trans} and v_p inside all the components for each DCE-MRI slice, such as NC, CA, Hem, LM, and FIB, are reported.

Data Analysis

The analysis procedure was applied to the index carotid artery of each subject, using both AIF approaches. For each component, the mean values and 95% confidence intervals of K^{trans} and v_p are compared. To eliminate any potential overlap between NC and Hem, which generally occurs within the NC, the NC analysis was limited to regions that did not contain Hem. The nonparametric comparison (Mann-Whitney U test) was used to compare the significance of differences between components in K^{trans} and v_p, with P values below 0.05 considered significant.

RESULTS

Of the original 55 subjects, eight subjects were excluded because the DCE imaging location missed the bifurcation of the index artery. For the remaining 47 subjects, 227 matched slices were available with DCE-MRI results and at least one plaque component drawn within the wall.

For performance of the automated registration algorithms, the correct longitudinal correspondence of slices was identified in 76.6% of 47 cases. The in-plane refinement of the lumen, wall, and component mapping was successful in 72.7% of slices, with the remainder requiring additional manual in-plane shift adjustment.

For the results using the directly measured AIF, the mean K^{trans} and v_p values for each component are

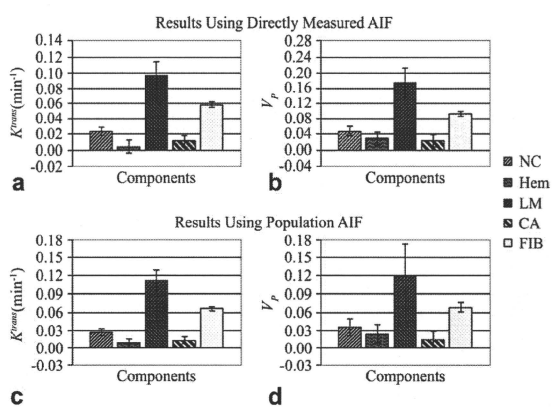

FIG. 3. Comparison of mean K^{trans} **(a)** and v_p **(b)** (columns) using directly measured AIF and their 95% confidence interval (bars) across different components. **c,d:** The comparison results using population-derived AIF.

Table 2
Statistical Comparison (Mann-Whitney U Test) of K^{trans} Produced by Directly Measured AIF Between Any Two of the Plaque Components (*P* Value)*

K^{trans} U test *P* value	NC	Hem	LM	CA	FIB
NC	1				
Hem	***<0.001***	1			
LM	***<0.001***	***<0.001***	1		
CA	***<0.001***	0.384	***<0.001***	1	
FIB	***<0.001***	***<0.001***	***<0.001***	***<0.001***	1

**P* value <0.05 for values in bold italic.

Table 4
Statistical Comparison (Mann-Whitney U Test) of K^{trans} Produced by Population-Derived AIF Between Any Two of the Plaque Components (*P* Value)*

K^{trans} U test *P* value	NC	Hem	LM	CA	FIB
NC	1				
Hem	***<0.001***	1			
LM	***<0.001***	***<0.001***	1		
CA	***<0.001***	0.630	***<0.001***	1	
FIB	***<0.001***	***<0.001***	***<0.001***	***<0.001***	1

**P* value <0.05 for values in bold italic.

illustrated in Fig. 3a,b. Statistical comparisons between any two of the components are summarized in Tables 2 and 3 for K^{trans} and v_p, respectively. LM and FIB have relatively high values of K^{trans} (LM: 0.0962 ± 0.0180 [mean ± 95% confidence interval], FIB: 0.0581 ± 0.0040) and v_p (LM: 0.1736 ± 0.0389, FIB: 0.0915 ± 0.0067). In contrast, NC, Hem, and CA have relatively low values of K^{trans} (NC: 0.0236 ± 0.0055, Hem: 0.0041 ± 0.0081, CA: 0.0111 ± 0.0069) and v_p (NC: 0.0475 ± 0.0118, Hem: 0.0288 ± 0.0161, CA: 0.0224 ± 0.0159). In paired comparison of K^{trans} and v_p, CA and Hem showed no significant differences between them, but the K^{trans} and v_p values for any other pair of components were significantly different.

The estimations using the population-derived AIF had similar results as those generated by the measured AIF. The mean K^{trans} and v_p values for each component are shown in Fig. 3c,d, again demonstrating relatively high values in LM and FIB (K^{trans}: LM: 0.1124 ± 0.0162, FIB: 0.0661 ± 0.0039; v_p: LM: 0.1201 ± 0.0533, FIB: 0.0682 ± 0.0079). Also, NC, Hem, and CA have relatively low values of K^{trans} (NC: 0.0270 ± 0.0053, Hem: 0.0077 ± 0.0074, CA: 0.0131 ± 0.0060) and v_p (NC: 0.0354 ± 0.0142, Hem: 0.0241 ± 0.0156, CA: 0.0138 ± 0.0144). In statistical comparisons between any two of the components (Table 4 for K^{trans} and Table 5 for v_p), CA and Hem also present no significant differences between them, while any other pair of components was significantly different in the K^{trans} and v_p values.

DISCUSSION AND CONCLUSIONS

The results of this analysis indicate that DCE-MRI exhibits differences in K^{trans} and v_p within plaque regions with different compositions, reflecting different permeability and vascular blood supply. LM is a loosely organized region of FIB with high water content and permeability that leads to the highest measured K^{trans} and v_p. FIB contains rich microvasculature with relatively high permeability, also leading to high K^{trans} and v_p. In contrast, NC, Hem, and CA do not generally contain living cells and exhibit little vascularization, leading to substantially lower values of K^{trans} and v_p.

One implication of this result is that the derived V-V image from DCE-MRI could be used in differentiating plaque composition. NC, Hem, and CA usually appears dark in V-V images, with very low K^{trans} and v_p. LM usually appears light green in V-V images, with highest K^{trans} and v_p. These characteristics could be added to those established for standard MRI contrast weightings (10) to potentially improve plaque characterization.

More significantly, with localized K^{trans} and v_p measurements, DCE-MRI has the ability to assess plaque perfusion characteristics in specific plaque regions. This may enable quantitative DCE-MRI to replace or augment the use of ultrasmall superparamagnetic particles of iron oxide, which localize the presence of macrophages in atherosclerotic plaque (15,16). This also may provide more localized information than positron emission tomography to evaluate the role of inflammation in atherosclerosis plaque progression and rupture. Previous studies have established that global perfusion characteristics are strongly dependent on global macrophage content (6) and systemic markers of inflammation (12). Assuming that local perfusion characteristics are primarily driven by local inflammatory cell content, localized K^{trans} and v_p measurements could be used to quantify inflammation where it is most likely to lead to plaque disruption. The shoulder region of the plaque could be one such region. A previous study (17) suggested that plaque rupture

Table 3
Statistical Comparison (Mann-Whitney U Test) of v_p Produced by Directly Measured AIF Between Any Two of the Plaque Components (*P* Value)*

v_p U test *P* value	NC	Hem	LM	CA	FIB
NC	1				
Hem	***0.020***	1			
LM	***<0.001***	***<0.001***	1		
CA	***0.006***	0.817	***<0.001***	1	
FIB	***<0.001***	***<0.001***	***<0.001***	***<0.001***	1

**P* value <0.05 for values in bold italic.

Table 5
Statistical Comparison (Mann-Whitney U Test) of v_p Produced by Population-Derived AIF Between Any Two of the Plaque Components (*P* Value)*

v_p U test *P* value	NC	Hem	LM	CA	FIB
NC	1				
Hem	***0.017***	1			
LM	***<0.001***	***<0.001***	1		
CA	***0.005***	0.679	***<0.001***	1	
FIB	***<0.001***	***<0.001***	***<0.001***	***<0.001***	1

**P* value <0.05 for values in bold italic.

occurs most frequently at regions heavily infiltrated by foam cells. Macrophages are capable of degrading the extracellular matrix by phagocytosis or by secreting proteolytic enzymes such as plasminogen activators and the family of matrix metalloproteinases, which may cause a rupture. These macrophages, together with the neovasculatures that facilitate the infiltration of the macrophages, are observed frequently in the plaque shoulders (18).

In this study, we sought to establish an automatic procedure to measure the localized K^{trans} reliably. Although the DCE-MRI images of some cases have bad image quality that has no clear lumen boundary and some cases have very big misalignment between DCE-MRI and other weightings due to the movements of patients, the success rate of the location registration algorithm is over 75%, and over 70% of all the slices do not need manual adjustment when mapping contours to V-V images. The result shows that the established registration algorithms are working and can avoid manual operation most of the time.

This study also compared the influence of two different AIF extraction methods: a cluster algorithm to directly measure the AIF from signal enhancement inside the blood vessel and a model-based population-derived AIF. Differences were observed, depending on the AIF methodology. In Fig. 3, we observe that average K^{trans} values are 15% higher with the population-derived AIF (median difference = 15%) and v_p is lower (median difference = 29%). Nevertheless, nearly identical relative values were observed when comparing modeling results from different tissue types. Thus, the choice of AIF methodology did not appear to alter the conclusion that variations in perfusion parameters are localizable within atherosclerotic plaque.

A limitation of this study is the lack of histologic data. Thus, the relative accuracies of the two AIF methodologies cannot be compared. Also, the hypothesis that localized measurements of K^{trans} and v_p indicate local inflammatory burden cannot be directly verified with histology. However, the result of this study was indirectly verified because the components used in this analysis were defined with a histologically verified protocol on multi-contrast MRI (10) and directly mapped to DCE-MRI, and DCE-MRI has been shown to be sensitive to inflammatory content within plaque in studies with histologic verification (6,7).

There are also some potential improvements in several technical areas. First, a dynamic protocol lasting about 3.8 min was chosen to not extend the already long scan protocol for carotid plaque imaging. The relatively short duration time requires us to use a linearized kinetic model that ignores efflux effect of the contrast agent (19) and avoids potential fit failures that often occur with more complicated models. However, the linearized model cannot differentiate the parameter for partial volume of extravascular extracellular space (v_e) and the transfer rate (K_{ep}) that compose K^{trans} (12). Second, to obtain sufficient coverage, signal-to-noise ratio and spatial resolution, we chose a relative long interval of 19 sec, which could affect the accuracy of the kinetic analysis by undersampling the AIF and tissue uptake curves. Further improvement on the temporal resolution could greatly benefit the kinetic analysis. Last, we assume the T_1-dependent signal intensity change in DCE images can be used in place of contrast agent concentration with the spoiled gradient recalled echo imaging sequence and saturation band used in this study. This may produce bias in the kinetic parameters. With further improvement such as measuring the change in longitudinal relaxation rate instead of signal intensity, we could indicate the concentration of contrast agent more accurately. Despite these technical limitations, we were able to demonstrate that kinetic parameters provide local information, a conclusion that is likely to apply to improved DCE techniques as well.

In conclusion, the results of this analysis indicate that DCE-MRI exhibits differences in K^{trans} within plaque regions of different compositions. If the results of further studies with histology verify the association between the derived parameters (K^{trans} and v_p) and inflammation in localized regions, DCE-MRI will be of value for studying the dependence of plaque progression and rupture on local inflammatory processes. Moreover, DCE-MRI could be useful for studies evaluating the effectiveness of novel therapies intended to inhibit plaque inflammation.

REFERENCES

1. Ross R. Atherosclerosis: an inflammatory disease. N Engl J Med 1999;340:115–126.
2. Libby P. Inflammation in atherosclerosis. Nature 2002;420:868–874.
3. Aikawa M, Rabkin E, Okada Y, Voglic SJ, Clinton SK, Brinckerhoff CE, Sukhova GK, Libby P. Lipid lowering by diet reduces matrix metalloproteinase activity and increases collagen content of rabbit atheroma: a potential mechanism of lesion stabilization. Circulation 1998;97:2433–2444.
4. Rudd JHF, Warburton EA, Fryer TD, Jones HA, Clark JC, Antoun N, Johnstrom P, Davenport AP, Kirkpatrick PJ, Arch BN, Pickard JD, Weissberg PL. Imaging atherosclerotic plaque inflammation with [18F]-fluorodeoxyglucose positron emission tomography. Circulation 2002;105:2708–2711.
5. Yuan C, Kerwin WS, Ferguson MS, Polissar N, Zhang S, Cai J, Hatsukami TS. Contrast enhanced high resolution MRI for atherosclerotic carotid artery tissue characterization. J Magn Reson Imaging 2002;15: 62–67.
6. Kerwin WS, O'Brien KD, Ferguson MS, Polissar N, Hatsukami TS, Yuan C. Inflammation in carotid atherosclerotic plaque: a dynamic contrast-enhanced MR imaging study. Radiology 2006;241:459–468.
7. Calcagno C, Cornily JC, Hyafil F, Rudd JHF, Briley-Saebo KC, Mani V, Goldschlager G, Machac J, Fuster V, Fayad ZA. Detection of neovessels in atherosclerotic plaques of rabbits using dynamic contrast enhanced MRI and 18F-FDG PET. Arterioscler Thromb Vasc Biol 2008;28:1311–1317.
8. Yarnykh VL, Yuan C. T1-insensitive flow suppression using quadruple inversion-recovery. Magn Reson Med 2002;48:899–905.
9. Yarnykh VL, Terashima M, Hayes CE, Shimakawa A, Takaya N, Nguyen PK, Brittain JH, McConnell MV, Yuan C. Multi-contrast black-blood MRI of carotid arteries: comparison between 1.5 and 3 tesla magnetic field strengths. J Magn Reson Imaging 2006;23: 691–698.
10. Saam T, Ferguson MS, Yarnykh VL, Takaya N, Xu D, Polissar NL, Hatsukami TS, Yuan C. Quantitative evaluation of carotid plaque composition by in vivo MRI. Arterioscler Thromb Vasc Biol 2005;25: 234–239.
11. Kerwin WS, Xu D, Liu F, Saam T, Underhill H, Takaya N, Chu B, Hatsukami TS, Yuan C. Magnetic resonance imaging of carotid atherosclerosis: plaque analysis. Top Magn Reson Imaging 2007;18: 371–378.
12. Kerwin WS, Oikawa M, Yuan C, Jarvik GP, Hatsukami TS. MR imaging of adventitial vasa vasorum in carotid atherosclerosis. Magn Reson Med 2008;59:507–514.

13. Schabel MC, Parker DL, Uncertainty and bias in contrast concentration measurements using spoiled gradient echo pulse sequences. Phys Med Biol 2008;53:2345–2373.
14. Wang Y, Huang W, Panicek DM, Schwartz LH, Koutcher JA. Feasibility of using limited-population-based arterial input function for pharmacokinetic modeling of osteosarcoma dynamic contrast-enhanced MRI data. Magn Reson Med 2008;59:1183–1189.
15. Kooi ME, Cappendijk VC, Cleutjens KBJM, Kessels AGH, Kitslaar PJEHM, Borgers M, Frederik PM, Daemen MJAP, van Engelshoven JMA. Accumulation of ultrasmall superparamagnetic particles of iron oxide in human atherosclerotic plaques can be detected by in vivo magnetic resonance imaging. Circulation 2003;107:2453–2458.
16. Trivedi RA, Mallawarachi C, U-King-Im JM, Graves MJ, Horsley J, Goddard MJ, Brown A, Wang L, Kirkpatrick PJ, Brown J, Gillard JH. Identifying inflamed carotid plaques using in vivo USPIO-enhanced MR imaging to label plaque macrophages. Arterioscler Thromb Vasc Biol 2006;26:1601–1606.
17. Falk E, Shah PK, Fuster V. Coronary plaque disruption. Circulation 1995;92:657–671.
18. Jeziorska M, Woolley DE. Local neovascularization and cellular composition within vulnerable regions of atherosclerotic plaques of human carotid arteries. J Pathol 1999;188:189–196.
19. Patlak CS, Blasberg RG, Fenstermacher JD. Graphical evaluation of blood-to-brain transfer constants from multiple-time uptake data. J Cereb Blood Flow Metab 1983;3:1–7.

ORIGINAL RESEARCH

A Noninvasive Imaging Approach to Assess Plaque Severity: The Carotid Atherosclerosis Score

H.R. Underhill
T.S. Hatsukami
J. Cai
W. Yu
J.K. DeMarco
N.L. Polissar
H. Ota
X. Zhao
L. Dong
M. Oikawa
C. Yuan

BACKGROUND AND PURPOSE: The presence of IPH and/or FCR in the carotid atherosclerotic plaque indicates a high-risk lesion. The aim of this multicenter cross-sectional study was to establish the characteristics of lesions that may precede IPH and/or FCR. We further sought to construct a CAS that stratifies carotid disease severity.

MATERIALS AND METHODS: Three hundred forty-four individuals from 4 imaging centers with 16%–99% carotid stenosis by duplex sonography underwent carotid MR imaging. In approximately 60% of the study sample (training group), multivariate analysis was used to determine factors associated with IPH and FCR. Statistically significant parameters identified during multivariate analysis were used to construct CAS. CAS was then applied to the remaining arteries (40%, test group), and the accuracy of classification for determining the presence versus absence of IPH or, separately, FCR was determined by ROC analysis and calculation of the AUC.

RESULTS: The maximum proportion of the arterial wall occupied by the LRNC was the strongest predictor of IPH ($P < .001$) and FCR ($P < .001$) during multivariate analysis of the training group. The subsequently derived CAS applied to the test group was an accurate classifier of IPH (AUC = 0.91) and FCR (AUC = 0.93). Compared with MRA stenosis, CAS was a stronger classifier of both IPH and FCR.

CONCLUSIONS: LRNC quantification may be an effective complementary strategy to stenosis for classifying carotid atherosclerotic disease severity. CAS forms the foundation for a simple imaging-based risk-stratification system in the carotid artery to classify severity of atherosclerotic disease.

ABBREVIATIONS: AH = Anzhen Hospital; AUC = area-under-the-curve; CAS = Carotid Atherosclerosis Score; CE = contrast-enhanced; CE-MRA = contrast-enhanced MR angiography; CE-T1WI = contrast-enhanced T1-weighted imaging; CI = confidence interval; FCR = fibrous cap rupture; FSE = fast spin-echo; FSPGR = fast SPGR; FSRS = Framingham Stroke Risk Score; IMT = intima-media thickness; Inf = infinite; IPH = intraplaque hemorrhage; JV = jugular vein; LRNC = lipid-rich necrotic core; Max = maximum; MDIR = multisection double inversion recovery; Min = minimum; MRA = MR angiography; MRI = MR imaging; MSU = Michigan State University; NWI = normalized wall index; OR = odds ratio; PD = proton density; PLA = People's Liberation Army General Hospital; QIR = quadruple inversion recovery; ROC = receiver operating characteristics; SPGR = spoiled gradient-recalled echo; T1WI = T1-weighted imaging; T2WI = T2-weighted imaging; TOF = time-of-flight; TVA = total vessel area; UW = University of Washington

Carotid atherosclerotic disease is a leading cause of stroke. Disease severity and risk of stroke have been traditionally determined by measures of luminal occlusion.[1] Findings from randomized prospective investigations, however, have indicated that stenosis may be an uncertain measure of stroke risk in symptomatic patients with <70% stenosis[2] and across all levels of stenoses in asymptomatic patients.[3] Concurrently, atherosclerotic plaques in the coronary arteries associated with sudden cardiac death have been differentiated from lesions not associated with infarcts by histologic findings from within the vessel wall.[4] In accord, considerable effort has been directed at identifying features of the carotid arterial wall that may provide complementary information to lumenography to evaluate disease severity better.

MR imaging of the carotid arteries has been validated with histology to be an effective method to identify and measure atherosclerotic vessel morphology and plaque composition.[5-7] Recent carotid MR imaging–based cross-sectional[8-10] and prospective[11-13] studies of carotid atherosclerosis have offered exciting evidence that among many plaque features, IPH and FCR are some of the key determinants of the high-risk lesion—plaques associated with cerebrovascular events. Beyond the differentiation of high-risk lesions, however, a critical component of disease assessment is the recognition of lesions that may precede the development of IPH and/or FCR. The aim of this multicenter cross-sectional study was to determine which imaging features or combination of imaging features

Received June 19, 2009; accepted after revision November 23.

From the Departments of Radiology (H.R.U., X.Z., L.D., M.O., C.Y.) and Surgery (T.S.H.), University of Washington, Seattle, Washington; Department of Radiology (J.C.), People's Liberation Army General Hospital, Beijing, China; Department of Radiology (W.Y.), Anzhen Hospital, Capital Medical University, Beijing, China; Department of Radiology (J.K.D., H.O.), Michigan State University, East Lansing, Michigan; and Mountain-Whisper-Light Statistical Consulting (N.L.P.), Seattle, Washington.

This work was supported by grants from the National Institutes of Health (R01-HL56874, R01-HL073401, P01-HL072262, R01-HL61851), the American Heart Association's Midwest Affiliate Grant-in-Aid (0855604G), and Michigan State University (OVPRGS 05-IRGP-472).

Please address correspondence to Hunter R. Underhill, MD, Vascular Imaging Lab, University of Washington, 815 Mercer St, Box 358050, Seattle, WA 98109; e-mail: hunterru@u.washington.edu

Indicates open access to non-subscribers at www.ajnr.org

Indicates article with supplemental on-line tables.

DOI 10.3174/ajnr.A2007